# 12 The weak interactions of leptons

In the previous chapter, the general structure of the charged-current weak interaction was introduced. In this chapter, these ideas are applied to the weak interactions of charged leptons and neutrinos. The scattering cross sections for neutrinos on nucleons are calculated from first principles and the experimental measurements are related to the nucleon parton distribution functions. In the final section, the high-energy charged-current process $e^-p \to \nu_e X$ is used as an example of the weak interaction in the limit $Q^2 > m_W^2$.

## 12.1 Lepton universality

From the observed decay rates of muons and tau leptons, it is found that the strength of the weak interaction is the same for all lepton flavours. For example, Figure 12.1 shows the Feynman diagram for muon decay, $\mu^- \to e^-\overline{\nu}_e\nu_\mu$. It involves two weak-interaction vertices, $\mu^-\nu_\mu W$ and $We^-\overline{\nu}_e$. In principle, the coupling at these two vertices could be different. Allowing for this possibility, the muon decay rate of (11.16) can be written

$$\Gamma(\mu^- \to e^-\overline{\nu}_e\nu_\mu) \equiv \frac{1}{\tau_\mu} = \frac{G_F^{(e)}G_F^{(\mu)}m_\mu^5}{192\pi^3}, \tag{12.1}$$

where the weak couplings to the electron and muon are respectively $G_F^{(e)}$ and $G_F^{(\mu)}$.

The same calculation for the decay rate $\tau^- \to e^-\overline{\nu}_e\nu_\tau$ gives

$$\Gamma(\tau^- \to e^-\overline{\nu}_e\nu_\tau) = \frac{G_F^{(e)}G_F^{(\tau)}m_\tau^5}{192\pi^3}. \tag{12.2}$$

The tau-lepton is sufficiently massive that it can also decay into a muon or to mesons formed from light quarks, as shown in Figure 12.2. Therefore the tau lifetime needs to expressed in terms of the total decay rate

$$\frac{1}{\tau_\tau} = \Gamma = \sum_i \Gamma_i,$$

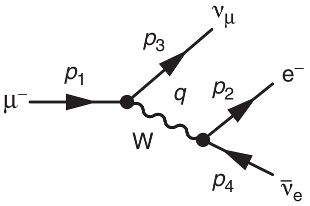

Fig. 12.1 The lowest-order Feynman diagram for muon decay.

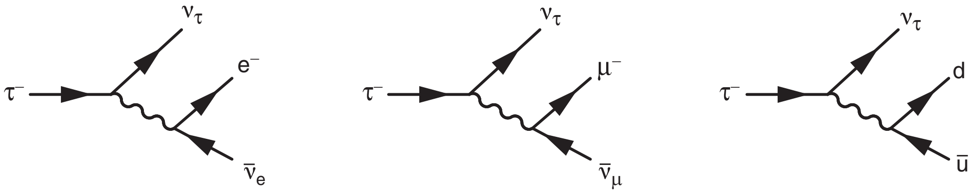

Fig. 12.2 The lowest-order Feynman diagrams for tau decay.

where $\Gamma_i$ are the partial decay rates for the individual decay modes. The ratio of the partial width $\Gamma(\tau^- \to e^-\overline{\nu}_e\nu_\tau)$ to the total decay rate gives the branching ratio

$$Br(\tau^- \to e^-\overline{\nu}_e\nu_\tau) = \frac{\Gamma(\tau^- \to e^-\overline{\nu}_e\nu_\tau)}{\Gamma} = \Gamma(\tau^- \to e^-\overline{\nu}_e\nu_\tau) \times \tau_\tau. \tag{12.3}$$

From (12.2) and (12.3), the tau lifetime can be expressed as

$$\tau_\tau = \frac{192\pi^3}{G_F^{(e)}G_F^{(\tau)}m_\tau^5} Br(\tau^- \to e^-\overline{\nu}_e\nu_\tau). \tag{12.4}$$

Comparing the expressions for the muon and tau-lepton lifetimes given in (12.1) and (12.4), gives the ratio

$$\frac{G_F^{(\tau)}}{G_F^{(\mu)}} = \frac{m_\mu^5\tau_\mu}{m_\tau^5\tau_\tau} Br(\tau^- \to e^-\overline{\nu}_e\nu_\tau). \tag{12.5}$$

The ratios of the couplings can be obtained from the measured branching ratios for the leptonic decays of the tau-lepton, which are

$$Br(\tau^- \to e^-\overline{\nu}_e\nu_\tau) = 0.1783(5) \quad \text{and} \quad Br(\tau^- \to \mu^-\overline{\nu}_\mu\nu_\tau) = 0.1741(4),$$

and the measured masses and lifetimes of the muon and tau-lepton,

$$m_\mu = 0.1056583715(35)\,\text{GeV} \quad \text{and} \quad \tau_\mu = 2.1969811(22) \times 10^{-6}\,\text{s},$$
$$m_\tau = 1.77682(16)\,\text{GeV} \quad \text{and} \quad \tau_\tau = 0.2906(10) \times 10^{-12}\,\text{s}.$$

From these measured values and the relation of (12.5), the ratio of the muon and tau weak charged-current coupling strengths is determined to be

$$\boxed{\frac{G_\mathrm{F}^{(\tau)}}{G_\mathrm{F}^{(\mu)}} = 1.0023 \pm 0.0033.}$$

Similarly, by comparing $Br(\tau^- \to e^-\overline{\nu}_e\nu_\tau)$ to $Br(\tau^- \to \mu^-\overline{\nu}_\mu\nu_\tau)$, taking into account the expected small difference due to phase space, gives

$$\boxed{\frac{G_\mathrm{F}^{(e)}}{G_\mathrm{F}^{(\mu)}} = 1.000 \pm 0.004.}$$

Therefore, within the accuracy of the experimental measurements, it can be concluded that $G_\mathrm{F}^{(e)} = G_\mathrm{F}^{(\mu)} = G_\mathrm{F}^{(\tau)}$, providing strong experimental evidence for the lepton universality of the weak charged current; there is a universal coupling strength at the $We\nu_e$, $W\mu\nu_\mu$ and $W\tau\nu_\tau$ interaction vertices.

## 12.2 Neutrino scattering

Although neutrinos interact only weakly in matter, precise measurements of their properties can be made using sufficiently intense neutrino beams. The general scheme for producing a collimated beam of neutrinos is shown schematically in Figure 12.3. The neutrino beam is produced by firing an intense beam of high-energy protons at a target, resulting in a large flux of high-energy hadrons from the hard QCD interaction and subsequent hadronisation process. A significant fraction of the produced hadrons are charged pions, both $\pi^+$ and $\pi^-$. The charged pions of a particular charge sign can be focussed in the magnetic field generated by one or more “neutrino horns"; the other charge will be defocussed. In this way it is possible to produce a collimated beam of pions with a particular charge sign. The pion

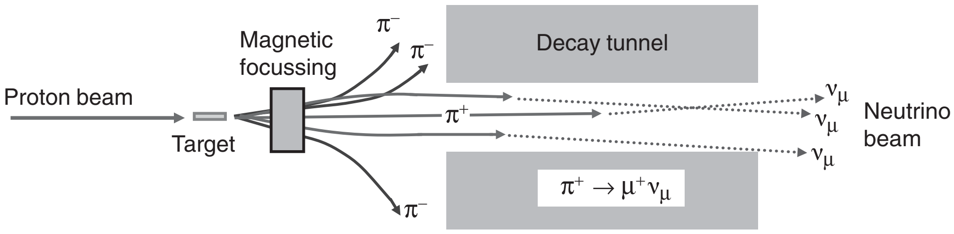

Fig. 12.3 The general scheme for producing a neutrino beam from a proton beam. The focussed pions produced from the target are allowed to decay in a long decay tunnel.

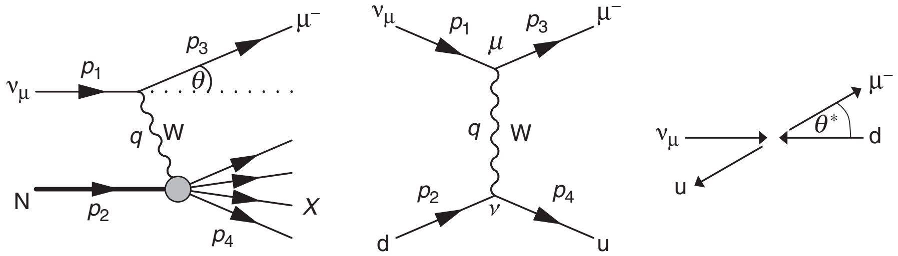

Fig. 12.4 Neutrino deep inelastic scattering and the Feynman diagram for the corresponding $\nu_\mu$d process. In the centre-of-mass frame the $\mu^-$ is produced at an angle $\theta^*$ to the incoming neutrino direction.

beam is then allowed to decay in flight over a distance of order $\gamma c\tau_\pi$ in an evacuated decay tunnel, which is typically a few hundred metres long. Because the mass of the pion is small compared to the typical pion energy, the neutrinos produced in the $\pi^+ \to \mu^+\nu_\mu$ or $\pi^- \to \mu^-\overline{\nu}_\mu$ decays are boosted along the direction of motion of the pions. The choice of the sense of the magnetic field in the neutrino horns enables either $\pi^+$ or $\pi^-$ to be focussed, and therefore either a $\nu_\mu$ or $\overline{\nu}_\mu$ beam can be produced. The muons produced from the pion decays are stopped in the rock at the end of the decay tunnel, before they decay themselves. The result is a collimated beam of almost entirely muon neutrinos or muon antineutrinos.

The phenomenology of neutrino scattering closely follows that of electron–proton scattering, discussed in Chapter 8. At low $Q^2$, there is a quasi-elastic process, $\nu_\mu n \to \mu^- p$, which is quasi-elastic in the sense that the nucleon changes type but does not break up. At slightly higher neutrino energies (a few GeV), resonant inelastic processes such as $\nu_\mu n \to \mu^-\Delta^+ \to \mu^- p\pi^0$ are observed. At higher energies still, neutrino interactions are dominated by the neutrino deep inelastic scattering process, shown in Figure 12.4.

In the neutrino scattering experiments considered in this chapter, the neutrino energy is sufficiently high that only the deep inelastic process is of relevance. For a neutrino interacting with a nucleon at rest, the centre-of-mass energy squared is

$$s = (p_1 + p_2)^2 = (E_\nu + m_N)^2 - E_\nu^2 = 2m_N E_\nu + m_N^2, \tag{12.6}$$

where $m_N$ is the mass of the nucleon. The maximum $Q^2$ in the scattering process is restricted by

$$Q^2 = (s - m_N^2)xy = 2m_N E_\nu xy,$$

and since $x$ and $y$ are always less than or equal to one, for a given neutrino energy,

$$Q^2 \le 2m_N E_\nu.$$

The highest-energy neutrinos produced in an accelerator-based neutrino beam had $E_\nu = 400\,\text{GeV}$, for which $Q^2 \lesssim 750\,\text{GeV}^2$. This is sufficiently small that, for all practical purposes, the weak interaction propagator can be approximated by

$$\frac{-ig_{\mu\nu}}{q^2 - m_W^2} \to \frac{ig_{\mu\nu}}{m_W^2}.$$

Furthermore, for high-energy neutrino interactions where the $m_N^2$ term in (12.6) can be neglected, the centre-of-mass energy squared is proportional to the neutrino energy,

$$s \approx 2m_N E_\nu. \tag{12.7}$$

The underlying interactions in neutrino–nucleon scattering are the parton-level processes, $\nu_\mu d \to \mu^- u$ and $\nu_\mu \overline{u} \to \mu^- \overline{d}$. The cross sections for these processes are calculated below. Because only left-handed chiral particle states and right-handed chiral antiparticle states participate in the weak charged-current, only one helicity combination needs to be considered in each case.

### 12.2.1 Neutrino–quark scattering cross section

Neglecting the $q^2$ dependence of the propagator, the matrix element for the Feynman diagram of Figure 12.4 is

$$\begin{aligned} -i\mathcal{M}_{fi} &= \left[-i\frac{g_W}{\sqrt{2}}\overline{u}(p_3)\gamma^\mu \tfrac{1}{2}(1-\gamma^5)u(p_1)\right]\frac{ig_{\mu\nu}}{m_W^2}\left[-i\frac{g_W}{\sqrt{2}}\overline{u}(p_4)\gamma^\nu \tfrac{1}{2}(1-\gamma^5)u(p_2)\right] \\ \mathcal{M}_{fi} &= \frac{g_W^2}{2m_W^2}g_{\mu\nu}\left[\overline{u}(p_3)\gamma^\mu \tfrac{1}{2}(1-\gamma^5)u(p_1)\right]\left[\overline{u}(p_4)\gamma^\nu \tfrac{1}{2}(1-\gamma^5)u(p_2)\right]. \end{aligned} \tag{12.8}$$

For high-energy neutrino scattering, both the masses of the neutrinos and quarks are sufficiently small that the LH chiral states are effectively identical to the LH helicity states and (12.8) can be written

$$\mathcal{M}_{fi} = \frac{g_W^2}{2m_W^2}g_{\mu\nu}\left[\overline{u}_\downarrow(p_3)\gamma^\mu u_\downarrow(p_1)\right]\left[\overline{u}_\downarrow(p_4)\gamma^\nu u_\downarrow(p_2)\right] = \frac{g_W^2}{2m_W^2}\, j_\ell \cdot j_q, \tag{12.9}$$

where $j_\ell^\mu = \overline{u}_\downarrow(p_3)\gamma^\mu u_\downarrow(p_1)$ and $j_q^\nu = \overline{u}_\downarrow(p_4)\gamma^\nu u_\downarrow(p_2)$ are respectively the lepton and quark currents.

The matrix element is most easily evaluated in the centre-of-mass frame. Taking the initial neutrino direction to define the $z$-axis and $\theta^*$ to be the polar angle of the

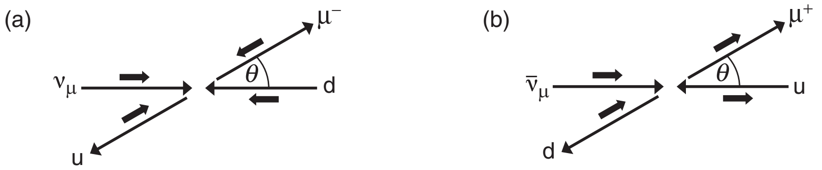

**Fig. 12.5** The spin orientations of the particles in (a) charged-current $\nu_\mu d \to \mu^- u$ and (b) charged-current $\overline{\nu}_\mu u \to \mu^+ d$ weak interactions.

final-state $\mu^-$, then the spherical polar angles of the four particles, as indicated in Figure 12.4, are

$$(\theta_1, \phi_1) = (0, 0), \quad (\theta_2, \phi_2) = (\pi, \pi), \quad (\theta_3, \phi_3) = (\theta^*, 0) \text{ and } (\theta_4, \phi_4) = (\pi - \theta^*, \pi).$$

The corresponding LH spinors are given by (4.67),

$$u_\downarrow(p_1) = \sqrt{E}\begin{pmatrix}0\\1\\0\\-1\end{pmatrix}, \; u_\downarrow(p_2) = \sqrt{E}\begin{pmatrix}-1\\0\\1\\0\end{pmatrix}, \; u_\downarrow(p_3) = \sqrt{E}\begin{pmatrix}-s\\c\\s\\-c\end{pmatrix} \; u_\downarrow(p_4) = \sqrt{E}\begin{pmatrix}-c\\-s\\c\\s\end{pmatrix}, \tag{12.10}$$

where $c = \cos\frac{\theta^*}{2}$, $s = \sin\frac{\theta^*}{2}$ and $E$ is the energy of each of the four particles in the centre-of-mass frame. The lepton and quark currents then can be evaluated by using the relations of (6.12)–(6.15), giving

$$j_\ell^\mu = \overline{u}_\downarrow(p_3)\gamma^\mu u_\downarrow(p_1) = 2E(c, s, -is, c),$$
$$j_q^\nu = \overline{u}_\downarrow(p_4)\gamma^\nu u_\downarrow(p_2) = 2E(c, -s, -is, -c),$$

and hence

$$\mathcal{M}_{fi} = \frac{g_W^2}{2m_W^2}\, j_\ell \cdot j_q = \frac{g_W^2}{2m_W^2} 4E^2(c^2 + s^2 + s^2 + c^2).$$

Therefore, the matrix element for $\nu_\mu d \to \mu^- u$ scattering is simply

$$\boxed{\mathcal{M}_{fi} = \frac{g_W^2}{m_W^2}\hat{s},} \tag{12.11}$$

where $\hat{s} = (2E)^2$ is the $\nu_\mu d$ centre-of-mass energy. The matrix element of (12.11) does not depend on the polar angle $\theta^*$ and therefore represents an isotropic distribution of the final-state particles in the centre-of-mass frame. This can be understood in terms of the helicities of the colliding particles, shown in Figure 12.5a. Because both the quark and neutrino are left-handed, the interaction occurs in an $S_z = 0$ state and thus there is no preferred polar angle in the centre-of-mass frame.

In the limit where the particle masses can be neglected, the centre-of-mass frame differential cross section is given by (3.50),

$$\frac{\mathrm{d}\sigma}{\mathrm{d}\Omega^*} = \frac{1}{64\pi^2 \hat{s}}\langle|\mathcal{M}_{fi}|^2\rangle,$$

where $\langle|\mathcal{M}_{fi}|^2\rangle$ is the spin-averaged matrix element squared. In this weak charged-current process, the only non-zero matrix element is that for the helicity combination $LL \to LL$, calculated above. Previously the average over the spins of the two initial-state fermions gave rise to a factor 1/4 in the spin-averaged matrix element. Here, because it was produced in a weak decay, the neutrino will always be left-handed and it is only necessary to average over the two spin states of the quark. Hence the spin-averaged matrix element squared is

$$\langle|\mathcal{M}_{fi}|^2\rangle = \frac{1}{2}\left(\frac{g_{\mathrm{W}}^2}{m_{\mathrm{W}}^2}\hat{s}\right)^2, \tag{12.12}$$

and the differential cross section is

$$\frac{\mathrm{d}\sigma}{\mathrm{d}\Omega^*} = \frac{1}{64\pi^2 \hat{s}}\langle|\mathcal{M}_{fi}|^2\rangle = \left(\frac{g_{\mathrm{W}}^2}{8\sqrt{2}\pi m_{\mathrm{W}}^2}\right)^2 \hat{s}.$$

Using $G_{\mathrm{F}} = \sqrt{2}g_{\mathrm{W}}^2/8m_{\mathrm{W}}^2$, this can be written as

$$\boxed{\frac{\mathrm{d}\sigma_{\nu\mathrm{q}}}{\mathrm{d}\Omega^*} = \frac{G_{\mathrm{F}}^2}{4\pi^2}\hat{s},} \tag{12.13}$$

and the total cross section, obtained by integrating over $\mathrm{d}\Omega^*$, is

$$\boxed{\sigma_{\nu\mathrm{q}} = \frac{G_{\mathrm{F}}^2\hat{s}}{\pi}.} \tag{12.14}$$

### 12.2.2 Antineutrino–quark scattering

Figure 12.6 shows the Feynman diagram for antineutrino–quark scattering. In order to conserve electric charge, the antineutrino can interact with an up-quark, but not a down-quark. The corresponding matrix element is

$$\mathcal{M}_{fi} = \frac{g_{\mathrm{W}}^2}{2m_{\mathrm{W}}^2} g_{\mu\nu}\left[\overline{v}(p_1)\gamma^{\mu}\tfrac{1}{2}(1-\gamma^5)v(p_3)\right]\left[\overline{u}(p_4)\gamma^{\nu}\tfrac{1}{2}(1-\gamma^5)u(p_2)\right].$$

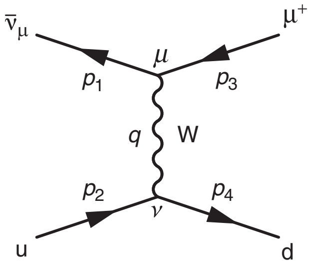

Fig. 12.6 The Feynman diagram for $\overline{\nu}_\mu u \to \mu^+ d$.

In the high-energy limit, only LH helicity particles and RH helicity antiparticles participate in the charged-current weak interaction and thus the only non-zero matrix element is given by

$$\mathcal{M}_{fi} = \frac{g_W^2}{2m_W^2} g_{\mu\nu} \left[\overline{v}_\uparrow(p_1)\gamma^\mu v_\uparrow(p_3)\right] \left[\overline{u}_\downarrow(p_4)\gamma^\nu u_\downarrow(p_2)\right].$$

Proceeding as before, it is straightforward to show that this leads to

$$\mathcal{M}_{\overline{\nu}q} = \tfrac{1}{2}(1+\cos\theta^*)\frac{g_W^2}{m_W^2}\hat{s}, \tag{12.15}$$

where $\theta^*$ is the polar angle of the $\mu^+$ in the centre-of-mass frame. This matrix element differs from the corresponding matrix element for neutrino–quark scattering (12.11) by the factor $\frac{1}{2}(1+\cos\theta^*)$. The origin of this difference can be understood in terms of spins of the particles, as shown in Figure 12.5b. The $V-A$ nature of the weak interaction means that the $\overline{\nu}q$ interaction occurs in an $S_z = 1$ state and, from the discussion of Section 6.3, this results in an angular dependence of the matrix element of $\frac{1}{2}(1+\cos\theta^*)$. Therefore, the $\overline{\nu}_\mu u$ differential cross section is related to that for $\nu_\mu d$ by

$$\frac{d\sigma_{\overline{\nu}q}}{d\Omega^*} = \tfrac{1}{4}(1+\cos\theta^*)^2\frac{d\sigma_{\nu q}}{d\Omega^*} = \frac{G_F^2}{16\pi^2}(1+\cos\theta^*)^2\hat{s},$$

and the total cross section is obtained by integrating over solid angle with

$$\int (1+\cos\theta^*)^2 d\Omega^* = \int_0^{2\pi} d\phi^* \int_{-1}^{+1}(1+x)^2 dx = \frac{16\pi}{3},$$

where the substitution $x = \cos\theta^*$ was used. Hence, the total antineutrino–quark cross section is

$$\sigma_{\overline{\nu}q} = \frac{G_F^2\hat{s}}{3\pi},$$

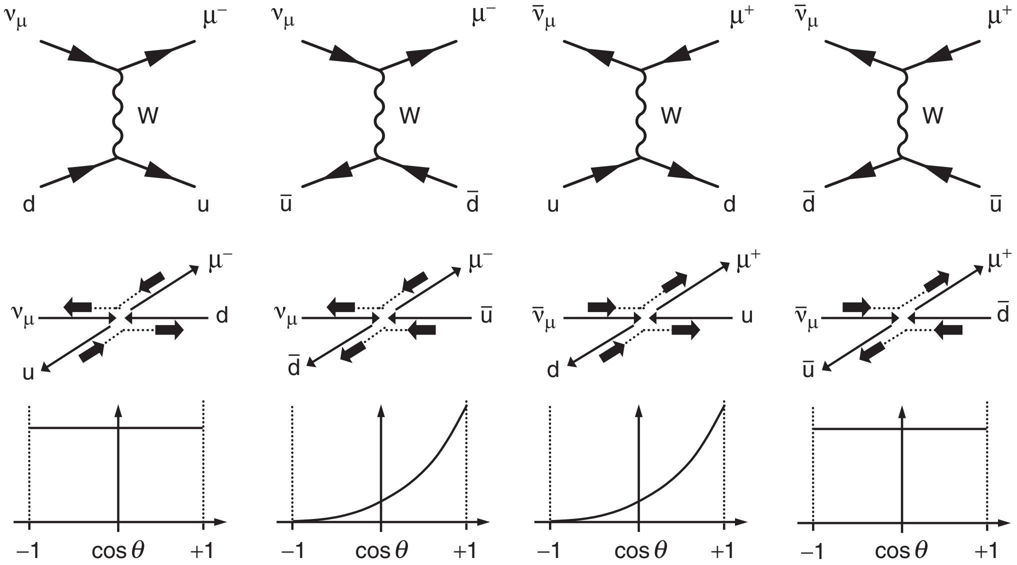

Fig. 12.7 The four possible Feynman diagrams and corresponding helicity combinations for the weak charged-current interactions involving $\nu_\mu$, $\overline{\nu}_\mu$ and any light (ud) quark or antiquark. Also shown are the corresponding angular distributions in the centre-of-mass frame.

which is a factor three smaller than the neutrino–quark cross section

$$\boxed{\frac{\sigma_{\overline{\nu}q}}{\sigma_{\nu q}} = \frac{1}{3}.}$$

### Neutrino–nucleon differential cross sections

Neutrino interactions in matter are described by their interactions with the constituent quarks of nucleons. From the conservation of electric charge, there are only four possible interactions between a $\nu_\mu$ or $\overline{\nu}_\mu$ and the light constituents (u, d, $\overline{\mathrm{u}}$ and $\overline{\mathrm{d}}$) of the nucleon. These are $\nu_\mu \mathrm{d} \to \mu^-\mathrm{u}$, $\nu_\mu\overline{\mathrm{u}} \to \mu^-\overline{\mathrm{d}}$, $\overline{\nu}_\mu \mathrm{u} \to \mu^-\mathrm{d}$ and $\overline{\nu}_\mu\overline{\mathrm{d}} \to \mu^+\overline{\mathrm{u}}$. For each process only one helicity combination is involved. The differential cross sections for scattering from the antiquarks can be obtained directly from those derived above by considering the spin state in which the interaction occurs, as shown in Figure 12.7. The differential cross section for neutrino/antineutrino scattering from antiquarks can be equated to the corresponding scattering cross section for quarks that occurs in the same spin state. Hence

$$\frac{d\sigma_{\overline{\nu}\overline{\mathrm{d}}}}{d\Omega^*} = \frac{d\sigma_{\nu\mathrm{d}}}{d\Omega^*} = \frac{G_F^2\hat{s}}{4\pi^2} \quad \text{and} \quad \frac{d\sigma_{\overline{\nu}\mathrm{u}}}{d\Omega^*} = \frac{d\sigma_{\nu\overline{\mathrm{u}}}}{d\Omega^*} = \frac{G_F^2\hat{s}}{16\pi^2}(1+\cos\theta^*)^2.$$

Writing $\mathrm{d}\Omega^* = \mathrm{d}\phi^*\mathrm{d}(\cos\theta^*)$ and integrating over the azimuthal angle gives

$$\frac{\mathrm{d}\sigma_{\overline{\nu}\overline{\mathrm{d}}}}{\mathrm{d}(\cos\theta^*)} = \frac{\mathrm{d}\sigma_{\nu\mathrm{d}}}{\mathrm{d}(\cos\theta^*)} = \frac{G_\mathrm{F}^2\hat{s}}{2\pi} \tag{12.16}$$

and

$$\frac{\mathrm{d}\sigma_{\overline{\nu}\mathrm{u}}}{\mathrm{d}(\cos\theta^*)} = \frac{\mathrm{d}\sigma_{\nu\overline{\mathrm{u}}}}{\mathrm{d}(\cos\theta^*)} = \frac{G_\mathrm{F}^2\hat{s}}{8\pi}(1+\cos\theta^*)^2. \tag{12.17}$$

The differential cross sections of (12.16) and (12.17) can be expressed in a Lorentz-invariant form using the Lorentz-invariant kinematic variable

$$y \equiv \frac{p_2\cdot q}{p_2\cdot p_1}.$$

The choice of $y$ is motivated by the fact that it related to the fraction of the neutrino energy carried by the observed final-state muon and it can be measured directly in neutrino scattering experiments. For elastic neutrino–quark scattering in the centre-of-mass frame, the four-momenta appearing in the expression for $y$ are

$$p_1 = (E,0,0,E), \quad p_2 = (E,0,0,-E) \quad \text{and} \quad p_3 = (E,0,E\sin\theta^*,E\cos\theta^*),$$

and therefore $y$ can be written as

$$y = \frac{p_2\cdot q}{p_2\cdot p_1} = \frac{p_2\cdot(p_1-p_3)}{p_2\cdot p_1} = \tfrac{1}{2}(1-\cos\theta^*).$$

Differentiating $y$ with respect to $\cos\theta^*$ gives

$$\frac{\mathrm{d}y}{\mathrm{d}(\cos\theta^*)} = -\frac{1}{2},$$

and thus

$$\frac{\mathrm{d}\sigma}{\mathrm{d}y} = \left|\frac{\mathrm{d}(\cos\theta^*)}{\mathrm{d}y}\right|\frac{\mathrm{d}\sigma}{\mathrm{d}(\cos\theta^*)} = 2\frac{\mathrm{d}\sigma}{\mathrm{d}(\cos\theta^*)},$$

and the differential cross section of (12.16) can be expressed as

$$\boxed{\frac{\mathrm{d}\sigma_{\nu\mathrm{q}}}{\mathrm{d}y} = \frac{\mathrm{d}\sigma_{\overline{\nu}\overline{\mathrm{q}}}}{\mathrm{d}y} = \frac{G_\mathrm{F}^2}{\pi}\hat{s}.} \tag{12.18}$$

Furthermore, using $(1-y) = \frac{1}{2}(1+\cos\theta^*)$, the Lorentz-invariant forms of the $\overline{\nu}\mathrm{q}$ and $\nu\overline{\mathrm{q}}$ differential cross sections of (12.17) are

$$\boxed{\frac{\mathrm{d}\sigma_{\overline{\nu}\mathrm{q}}}{\mathrm{d}y} = \frac{\mathrm{d}\sigma_{\nu\overline{\mathrm{q}}}}{\mathrm{d}y} = \frac{G_\mathrm{F}^2}{\pi}(1-y)^2\hat{s}.} \tag{12.19}$$

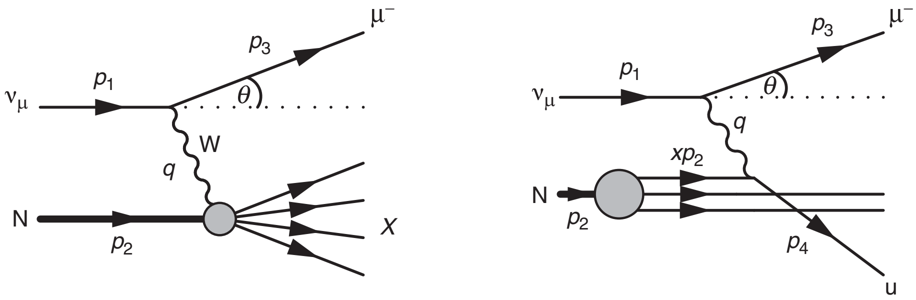

Fig. 12.8 The parton model picture of the charged-current scattering of a neutrino from a d quark in a nucleon.

### 12.2.3 Neutrino deep inelastic scattering

The interaction of high-energy neutrinos and antineutrinos with matter can be expressed in terms of deep inelastic scattering with protons and neutrons. The underlying interaction, shown in Figure 12.8, is between a neutrino/antineutrino and a quark/antiquark carrying a fraction $x$ of the nucleon momentum. Neglecting the contributions from the strange quark sea, the underlying physical processes for neutrino–proton deep inelastic scattering are $\nu_\mu \mathrm{d} \to \mu^- \mathrm{u}$ and $\nu_\mu \overline{\mathrm{u}} \to \mu^- \overline{\mathrm{d}}$ with differential cross sections given by (12.18) and (12.19). The number of down-quarks within a proton in the momentum fraction range $x \to x+\mathrm{d}x$ is $d(x)\,\mathrm{d}x$, where $d(x)$ is the down-quark parton distribution function for the proton. The equivalent expression for the anti-up-quarks is $\overline{u}(x)\,\mathrm{d}x$. The contribution to the total neutrino–proton scattering cross section from $\nu\mathrm{d}$ and $\nu\overline{\mathrm{u}}$ scattering is therefore

$$\frac{\mathrm{d}\sigma^{\nu\mathrm{p}}}{\mathrm{d}\hat{y}} = \frac{G_\mathrm{F}^2}{\pi}\hat{s}\left[d(x) + (1-\hat{y})^2\overline{u}(x)\right]\mathrm{d}x,$$

where $\hat{s}$ and $\hat{y}$ refer to the neutrino–quark system. The kinematic variables $\hat{s}$ and $\hat{y}$ can be expressed in terms of the neutrino–proton system using

$$\hat{s} = (p_1 + xp_2)^2 \approx 2xp_1 \cdot p_2 = xs \quad \text{and} \quad \hat{y} = \frac{p_q \cdot q}{p_q \cdot p_1} = \frac{xp_2 \cdot q}{xp_2 \cdot p_1} = y.$$

Hence, the parton model differential cross section for neutrino–proton scattering is

$$\frac{\mathrm{d}^2\sigma^{\nu\mathrm{p}}}{\mathrm{d}x\,\mathrm{d}y} = \frac{G_\mathrm{F}^2}{\pi} sx\left[d(x) + (1-y)^2\overline{u}(x)\right]. \tag{12.20}$$

The underlying processes for antineutrino–proton scattering are $\overline{\nu}\mathrm{u}$ and $\overline{\nu}\overline{\mathrm{d}}$ scattering, and the corresponding differential cross section is

$$\frac{\mathrm{d}^2\sigma^{\overline{\nu}\mathrm{p}}}{\mathrm{d}x\,\mathrm{d}y} = \frac{G_\mathrm{F}^2}{\pi} sx\left[(1-y)^2 u(x) + \overline{d}(x)\right]. \tag{12.21}$$

The differential cross sections for neutrino/antineutrino scattering with neutrons can be obtained from (12.20) and (12.21) by replacing the PDFs for the proton with those for the neutron, and using isospin symmetry to relate the neutron PDFs to those of the proton, $d^{\mathrm{n}}(x) = u(x)$, etc., giving

$$\frac{\mathrm{d}^2\sigma^{\nu\mathrm{n}}}{\mathrm{d}x\,\mathrm{d}y} = \frac{G_\mathrm{F}^2}{\pi}sx\left[u(x) + (1-y)^2\overline{d}(x)\right], \tag{12.22}$$

$$\frac{\mathrm{d}^2\sigma^{\overline{\nu}\mathrm{n}}}{\mathrm{d}x\,\mathrm{d}y} = \frac{G_\mathrm{F}^2}{\pi}sx\left[(1-y)^2 d(x) + \overline{u}(x)\right]. \tag{12.23}$$

In practice, because neutrino cross sections are so small, massive detectors are required. Consequently, the majority of the experiments that have studied high-energy neutrino deep inelastic scattering have employed detectors constructed from a dense material, usually steel (which is predominantly iron). Therefore, the measured neutrino cross sections are a combination of the cross sections for protons and neutrons. For an isoscalar target, with an equal number of protons and neutrons, the average neutrino scattering cross section per nucleon is

$$\frac{\mathrm{d}^2\sigma^{\nu\mathrm{N}}}{\mathrm{d}x\,\mathrm{d}y} = \frac{1}{2}\left(\frac{\mathrm{d}^2\sigma^{\nu\mathrm{p}}}{\mathrm{d}x\,\mathrm{d}y} + \frac{\mathrm{d}^2\sigma^{\nu\mathrm{n}}}{\mathrm{d}x\,\mathrm{d}y}\right),$$

which, from (12.20) and (12.22), can be written in terms of the PDFs as

$$\frac{\mathrm{d}^2\sigma^{\nu\mathrm{N}}}{\mathrm{d}x\,\mathrm{d}y} = \frac{G_\mathrm{F}^2 m_\mathrm{N}}{\pi}E_\nu\,x\left[d(x) + u(x) + (1-y)^2\left\{\overline{u}(x) + \overline{d}(x)\right\}\right], \tag{12.24}$$

where the centre-of-mass energy has been expressed in terms of the neutrino energy, $s \approx 2m_\mathrm{N}E_\nu$. The integral of (12.24) over the momentum fraction $x$ of the struck quark (or antiquark) gives the differential cross section in terms of $y$,

$$\frac{\mathrm{d}\sigma^{\nu\mathrm{N}}}{\mathrm{d}y} = \frac{G_\mathrm{F}^2 m_\mathrm{N}}{\pi}E_\nu\left[f_\mathrm{q} + (1-y)^2 f_{\overline{\mathrm{q}}}\right], \tag{12.25}$$

where $f_\mathrm{q}$ and $f_{\overline{\mathrm{q}}}$ are the fractions of the nucleon momentum respectively carried by the quarks and the antiquarks,

$$f_\mathrm{q} = \int_0^1 x\,[u(x) + d(x)]\,\mathrm{d}x \quad \text{and} \quad f_{\overline{\mathrm{q}}} = \int_0^1 x\left[\overline{u}(x) + \overline{d}(x)\right]\mathrm{d}x.$$

Likewise, the average antineutrino–nucleon scattering cross section, obtained from (12.21) and (12.23), is

$$\frac{\mathrm{d}^2\sigma^{\overline{\nu}\mathrm{N}}}{\mathrm{d}x\mathrm{d}y} = \frac{G_\mathrm{F}^2 m_\mathrm{N}}{\pi}E_\nu\,x\left[(1-y)^2\left\{u(x) + d(x)\right\} + \overline{u}(x) + \overline{d}(x)\right], \tag{12.26}$$

which when integrated over $x$ gives

$$\frac{\mathrm{d}\sigma^{\overline{\nu}\mathrm{N}}}{\mathrm{d}y} = \frac{G_{\mathrm{F}}^2 m_{\mathrm{N}}}{\pi} E_\nu \left[(1-y)^2 f_{\mathrm{q}} + f_{\overline{\mathrm{q}}}\right]. \tag{12.27}$$

Here the factor $(1-y)^2$ appears in front of the quark term rather than the antiquark term as in (12.25). The $y$-dependence of the differential cross sections for neutrino/antineutrino nucleon scattering can be utilised to provide a direct measurement of the antiquark content of the proton and neutron.

## 12.3 Neutrino scattering experiments

Over the past few decades there have been several high-energy neutrino beam experiments, such as the CDHS experiment at CERN, which took data from 1976 to 1984. The CDHS experiment used a collimated neutrino beam of either $\nu_\mu$ or $\overline{\nu}_\mu$ in the energy range 30 GeV–200 GeV, created from a 400 GeV proton beam. The neutrino interactions were observed in a detector with a mass of 1250 tons, which consisted of 19 magnetised iron modules, separated by wire drift chambers that provided a precise measurement of the position of the muon produced in charged-current neutrino interactions. The iron modules were built up of several iron plates with planes of plastic scintillator detectors in between them. The muon momentum was reconstructed from its curvature in the magnetic field of the detector and the energy of the final-state hadronic system was determined from the total energy deposited in the scintillator detectors between the iron plates.

An example of a charged-current $\nu_\mu$ interaction in the CDHS detector is shown in Figure 12.9. The upper half of the event display shows the deposited energy, as a function of distance along the detector. The energy deposition at the start of the interaction provides a measurement of the energy of the hadronic system, $E_X$.

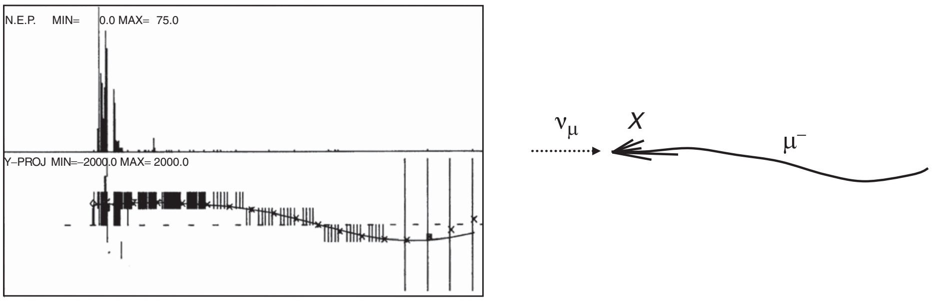

**Fig. 12.9** A deep inelastic neutrino interaction in the CDHS detector. The upper half of the left-hand plot shows the energy deposition as a function of depth in the detector and the lower half shows the precise position measurements provided by the drift chambers. The right-hand figure shows the interpretation of the event.

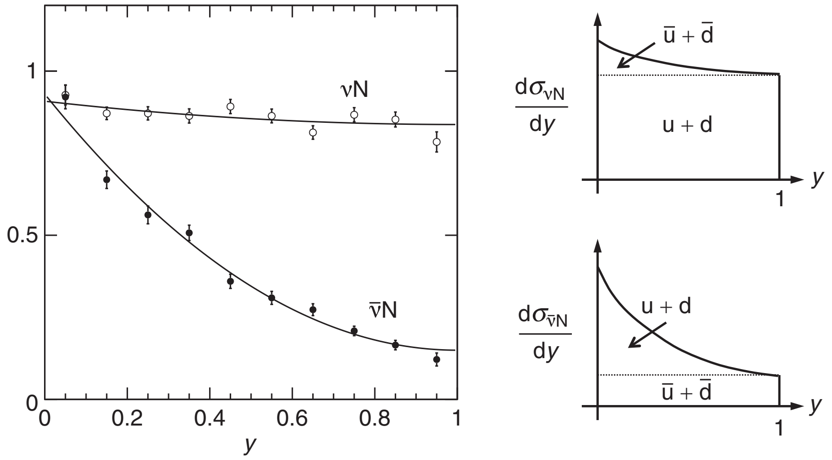

Fig. 12.10 The measured shape (arbitrary normalisation) of the νN and $\overline{\nu}$N differential cross sections from the CDHS experiment. Adapted from de Groot *et al.* (1979). The relative normalisation of the ν and $\overline{\nu}$ data have been corrected to correspond to the same flux. The plots on the right show the expected shapes of the measured differential cross sections in terms of quark and antiquark components.

The lower half of the event display shows the hit positions, from which the muon momentum can be reconstructed from the measured curvature. Thus, for each observed neutrino interaction, the neutrino energy can be reconstructed as

$$E_\nu = E_\mu + E_X,$$

and the value of $y$ for each interaction can be determined from (8.3),

$$y = \left(1 - \frac{E_\mu}{E_\nu}\right) = \frac{E_X}{E_X + E_\mu}.$$

The measured $y$-distributions for νN and $\overline{\nu}$N scattering from the CDHS experiment are shown in Figure 12.10. The data can be compared to expected distributions given in (12.25) and (12.27). The ν beam data show a clear contribution from νq scattering with a flat $y$ distribution and smaller contribution from ν$\overline{\text{q}}$ scattering with a $(1-y)^2$ distribution. The antineutrino data are dominated by the contribution from $\overline{\nu}$q scattering, which results in a $(1-y)^2$ distribution, with a smaller contribution from $\overline{\nu}\,\overline{\text{q}}$ scattering. Therefore the observed data can be understood in terms of a large quark component in the nucleon and a smaller antiquark component, as indicated in the plots on the left of Figure 12.10. The observed shapes of the measured $y$ distributions are consistent with the quarks carrying about five times the momentum fraction of the proton as the antiquarks.

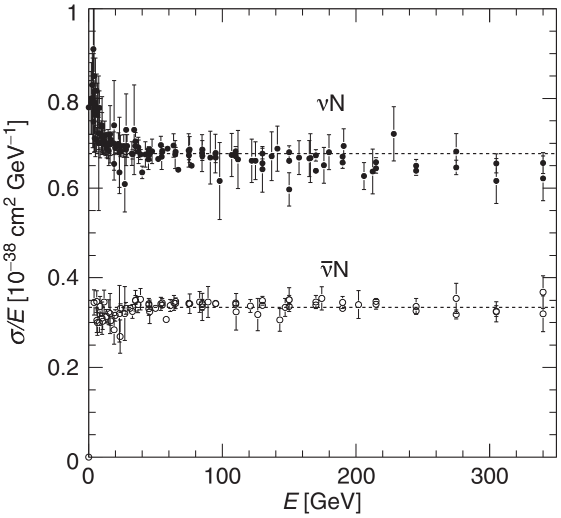

Fig. 12.11 A summary of the measurements of the total $\nu$N and $\overline{\nu}$N cross sections divided by the laboratory frame neutrino energy. The data are taken from references given in Beringer *et al.* (2012). The lines show the average values of the cross sections measured by a subset of the experiments in the range 30–200 GeV.

The total expected neutrino–nucleon cross section can be obtained by integrating (12.25) over $y$ to give

$$\sigma^{\nu N} = \frac{G_F^2 m_N E_\nu}{\pi}\left[f_q + \frac{1}{3}f_{\overline{q}}\right]. \tag{12.28}$$

Similarly, the integral of (12.27) gives the total antineutrino–nucleon cross section,

$$\sigma^{\overline{\nu} N} = \frac{G_F^2 m_N E_{\overline{\nu}}}{\pi}\left[\frac{1}{3}f_q + f_{\overline{q}}\right]. \tag{12.29}$$

The total neutrino deep inelastic cross section is proportional to the laboratory frame neutrino energy $E_\nu$, and the ratio of the $\nu$N to the $\overline{\nu}$N total cross section is

$$\frac{\sigma^{\nu N}}{\sigma^{\overline{\nu} N}} = \frac{3f_q + f_{\overline{q}}}{f_q + 3f_{\overline{q}}}. \tag{12.30}$$

Figure 12.11 summarises the experimental measurements of $\sigma^{\nu N}/E_\nu$ and $\sigma^{\overline{\nu} N}/E_{\overline{\nu}}$ for neutrino energies of up to 350 GeV. In the deep inelastic region, above about 30 GeV, the cross sections are approximately proportional to the neutrino energy and the measurements in the range 30–150 GeV are consistent with

$$\sigma^{\nu N}/E_\nu = 0.677 \pm 0.014 \times 10^{-38}\,\mathrm{cm^2\,GeV^{-1}}, \tag{12.31}$$

$$\sigma^{\overline{\nu} N}/E_{\overline{\nu}} = 0.334 \pm 0.008 \times 10^{-38}\,\mathrm{cm^2\,GeV^{-1}}, \tag{12.32}$$

giving the measured ratio

$$\frac{\sigma^{\nu\mathrm{N}}}{\sigma^{\overline{\nu}\mathrm{N}}} = 1.984 \pm 0.012.$$

If there were no antiquarks in the nucleon, the parton model prediction would be $\sigma^{\nu\mathrm{N}}/\sigma^{\overline{\nu}\mathrm{N}} = 3$. The presence of the antiquarks reduces this ratio to approximately two. The total cross section measurements of (12.31) and (12.32) can be interpreted as measurements of $f_\mathrm{q}$ and $f_{\overline{\mathrm{q}}}$ using the predicted deep inelastic cross sections of (12.28) and (12.29), giving

$$f_\mathrm{q} \approx 0.41 \quad \text{and} \quad f_{\overline{\mathrm{q}}} \approx 0.08.$$

Again, it is seen that only about half of the momentum of the proton is carried by the quarks/antiquarks, the remaining 50% is due to the gluons that do not interact with the W bosons of the weak interaction. Just under a tenth of momentum of the proton is carried by the antiquarks.

## 12.4 Structure functions in neutrino interactions

In the limit where particle masses can be neglected, the $\mathrm{e}^\pm\mathrm{p}$ deep inelastic cross section of (8.11) can be written in terms of $y$ as

$$\frac{\mathrm{d}^2\sigma^{\mathrm{e}^\pm\mathrm{p}}}{\mathrm{d}x\,\mathrm{d}y} = \frac{4\pi\alpha^2 s}{Q^4}\left[(1-y)\,F_2(x,Q^2) + y^2 x F_1(x,Q^2)\right], \tag{12.33}$$

where $F_1(x,Q^2)$ and $F_2(x,Q^2)$ are the structure functions described in Chapter 8. Equation (12.33) is the most general Lorentz-invariant *parity conserving* expression for the $\mathrm{e}^\pm\mathrm{p}$ cross section mediated by single photon exchange. The corresponding general expressions for neutrino/antineutrino deep inelastic scattering, which are modified to allow parity violation, are

$$\begin{aligned}
\frac{\mathrm{d}^2\sigma^{\nu\mathrm{p}}}{\mathrm{d}x\,\mathrm{d}y} &= \frac{G_\mathrm{F}^2 s}{2\pi}\left[(1-y)\,F_2^{\nu\mathrm{p}}(x,Q^2) + y^2 x F_1^{\nu\mathrm{p}}(x,Q^2) + y\left(1-\frac{y}{2}\right)xF_3^{\nu\mathrm{p}}(x,Q^2)\right],\\
\frac{\mathrm{d}^2\sigma^{\overline{\nu}\mathrm{p}}}{\mathrm{d}x\,\mathrm{d}y} &= \frac{G_\mathrm{F}^2 s}{2\pi}\left[(1-y)\,F_2^{\overline{\nu}\mathrm{p}}(x,Q^2) + y^2 x F_1^{\overline{\nu}\mathrm{p}}(x,Q^2) - y\left(1-\frac{y}{2}\right)xF_3^{\overline{\nu}\mathrm{p}}(x,Q^2)\right].
\end{aligned} \tag{12.34}$$

The structure functions are the experimental observables of deep inelastic scattering experiments that can then be interpreted in the parton model. By equating the

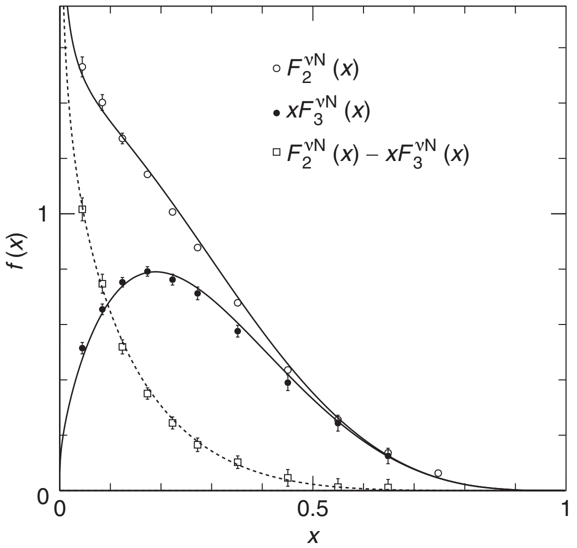

**Fig. 12.12** Measurements of $F_2^{\nu N}(x)$ and $xF_3^{\nu N}(x)$ in neutrino/antineutrino nucleon deep inelastic scattering in the NuTeV experiment at Fermilab for 7.5 GeV$^2$ $< Q^2 <$ 13.0 GeV$^2$, compared to the expected distributions from the parton distribution functions at $Q^2 = 10$ GeV$^2$ shown in Figure 8.17. Data from Tzanov *et al.* (2006).

powers of $y$ in (12.34) with those in the parton model prediction of (12.20), the structure functions can be expressed as

$$F_2^{\nu p} = 2xF_1^{\nu p} = 2x\left[d(x) + \overline{u}(x)\right],$$
$$xF_3^{\nu p} = 2x\left[d(x) - \overline{u}(x)\right].$$

The equivalent expressions for neutrino–nucleon scattering are

$$F_2^{\nu N} = 2xF_1^{\nu N} = \tfrac{1}{2}(F_2^{\nu p} + F_2^{\nu n}) = x\left[u(x) + d(x) + \overline{u}(x) + \overline{d}(x)\right], \qquad (12.35)$$
$$xF_3^{\nu N} = \tfrac{1}{2}(xF_3^{\nu p} + xF_3^{\nu n}) = x\left[u(x) + d(x) - \overline{u}(x) - \overline{d}(x)\right]. \qquad (12.36)$$

Using the parton model prediction that $F_2^{\nu N} = 2xF_1^{\nu N}$, the $y$-dependence of the cross sections can be expressed in terms of $F_2(x, Q^2)$ and $F_3(x, Q^2)$,

$$\frac{d^2\sigma^{\nu N}}{dx\,dy} = \frac{G_F^2 s}{2\pi}\left[\left(1 - y + \frac{y^2}{2}\right)F_2^{\nu N}(x, Q^2) + y\left(1 - \frac{y}{2}\right)xF_3^{\nu N}(x, Q^2)\right]. \qquad (12.37)$$

The structure functions, $F_2^{\nu N}(x, Q^2)$ and $F_3^{\nu N}(x, Q^2)$, can be obtained from the experimental measurements of the $y$-dependence of the measured neutrino cross sections at a particular value of $x$. For example, Figure 12.12 shows experimental measurements of $F_2^{\nu N}$ and $xF_3^{\nu N}$ at $Q^2 \sim 10\,\text{GeV}^2$ from the NuTeV experiment at Fermilab, which had a similar sandwich structure of steel plates and active detectors to the CDHS experiment described in Section 12.3. The data are compared to the predictions obtained using the PDFs shown in Figure 8.17, including the contribution from the strange quarks.

From (12.35) and (12.36), it can be seen that the difference

$$F_2^{\nu N}(x) - xF_3^{\nu N}(x) = 2x\left[\overline{u}(x) + \overline{d}(x)\right],$$

provides a direct measure of the antiquark content of the nucleon. The data of Figure 12.12 show clearly that the $x$ distribution of the antiquarks is, as expected, largest at low values of $x$. Furthermore, if the PDFs are written in terms of valence and sea quark contributions, it follows from (12.36) that

$$F_3^{\nu N}(x) = u_V(x) + d_V(x).$$

Therefore $F_3^{\nu N}(x)$ provides a direct measurement of the sum of the PDFs for the valence quarks alone. If there are three valence quarks within the nucleon, then

$$\int_0^1 F_3^{\nu N}(x)\,\mathrm{d}x = \int_0^1 u_V(x) + d_V(x)\,\mathrm{d}x = 3,$$

which is known as the Gross–Llewellyn-Smith sum rule. The measurement of $xF_3^{\nu N}(x)$, shown in Figure 12.12, is consistent with this prediction.

## 12.5 Charged-current electron–proton scattering

Section 8.5 described electron–proton scattering at a centre-of-mass energy of $\sqrt{s} = 300\,\mathrm{GeV}$ at the HERA collider. In addition to electron–proton collisions, which constituted the largest part of HERA operation, HERA also collided positrons and protons. For collisions at $Q^2 < m_W^2$, the $e^-p$ and $e^+p$ interactions are dominated by neutral-current QED $t$-channel deep inelastic scattering, mediated by photon exchange. However, since $Q^2 \approx sxy$, the $Q^2$ values obtainable at HERA extend above $m_W^2$. Therefore, for the interactions at the highest $Q^2$ values, charged-current scattering processes mediated by $W^\pm$ exchange, become increasingly important. Figure 12.13 shows the parton-level Feynman diagrams for the weak charged-current $e^-p \to \nu_e X$ and $e^+p \to \overline{\nu}_e X$ scattering processes. The experimental signature for high-$Q^2$ weak charged-current interactions is similar to the event shown in Figure 8.13, except that there is no final-state charged lepton. As

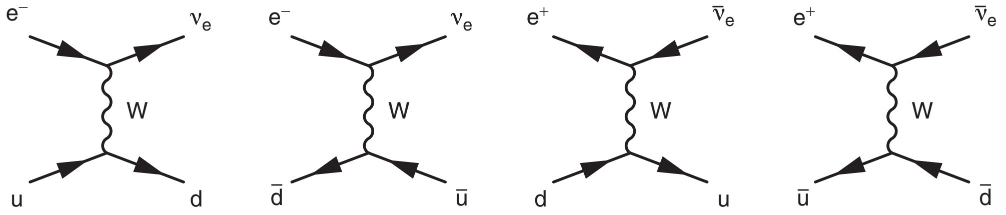

Fig. 12.13 Lowest-order diagrams contributing to charged-current $e^-p$ and $e^+p$ scattering.

discussed in Section 1.3, although the neutrino is not observed, its presence can be inferred from the momentum imbalance in the plane transverse to the beam axis. Consequently, the charged-current interactions mediated by the exchange of a W boson are clearly identifiable from the more common QED neutral-current interactions.

The calculations of the differential cross sections for charged current $e^-p$ and $e^+p$ scattering follow closely that for νp and $\bar{\nu}$p scattering described above. Consequently, the results can be obtained directly from the neutrino scattering cross sections by replacing the approximate low-$Q^2$ form of the W-boson propagator by

$$\frac{1}{m_W^2} \rightarrow \frac{1}{Q^2 + m_W^2},$$

and by making the replacement $u(x) \leftrightarrow d(x)$ and $u(x) \leftrightarrow d(x)$ to reflect the different quarks involved in the electron scattering interaction, which can be seen by comparing the Feynman diagrams of Figure 12.7 to those of Figure 12.13. With these replacements, the neutrino–proton cross section of (12.20) can be adapted to give the electron–proton weak charged-current scattering cross section,

$$\frac{d^2\sigma_{CC}^{e^-p}}{dx\,dy} = \frac{1}{2}\frac{G_F^2}{\pi}\frac{m_W^4}{(Q^2 + m_W^2)^2} sx\left(u(x) + (1-y)^2\bar{d}(x)\right), \tag{12.38}$$

where the additional factor of one-half comes from the need to average over the two spin states of the electron and quark, rather than just the quark spin in neutrino scattering. Using $Q^2 = sxy$, (12.38) can be written

$$\frac{d^2\sigma_{CC}^{e^-p}}{dx\,dQ^2} = \frac{d^2\sigma_{CC}^{e^-p}}{dx\,dy}\left|\frac{\partial y}{\partial Q^2}\right| = \frac{1}{sx}\frac{d^2\sigma_{CC}^{e^-p}}{dx\,dy}.$$

Hence the differential cross section for charged-current $e^-p \rightarrow \nu_e X$ scattering is

$$\frac{d^2\sigma_{CC}^{e^-p}}{dx\,dQ^2} = \frac{G_F^2 m_W^4}{2\pi(Q^2 + m_W^2)^2}\left(u(x) + (1-y)^2\bar{d}(x)\right), \tag{12.39}$$

and the corresponding expression for charged-current $e^+p \rightarrow \bar{\nu}_e X$ scattering is

$$\frac{d^2\sigma_{CC}^{e^+p}}{dx\,dQ^2} = \frac{G_F^2 m_W^4}{2\pi(Q^2 + m_W^2)^2}\left((1-y)^2 d(x) + \bar{u}(x)\right). \tag{12.40}$$

Figure 12.14 shows the measured charged-current and neutral-current differential cross sections for electron–proton and positron–proton scattering obtained by the H1 experiment at HERA. The main features of this plot can be understood in terms of the $Q^2$ dependence of the photon and W-boson propagators. For $Q^2 \ll m_W^2$, the W-boson propagator is approximately independent of $Q^2$,

$$1/(m_W^2 + Q^2) \approx 1/m_W^2,$$

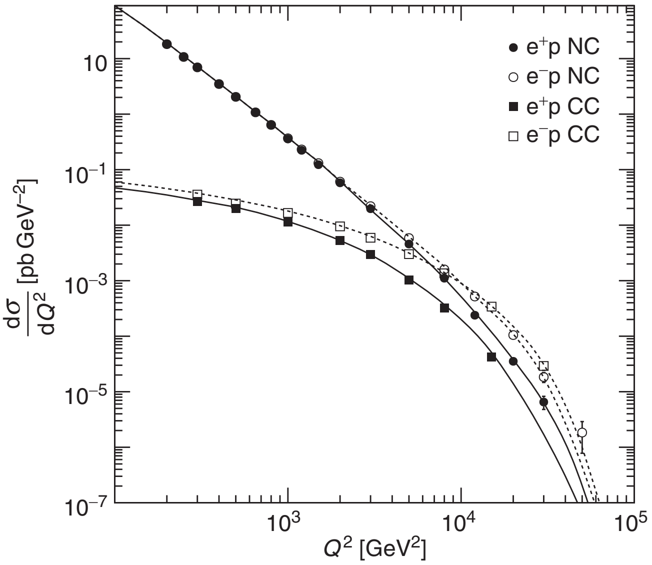

Fig. 12.14 The double-differential charged-current and neutral-current current cross sections for electron–proton and positron–proton scattering measured by the H1 experiment at $\sqrt{s} = 319$ GeV at the HERA collider. Adapted from data in Aaron *et al.* (2012).

which explains the relative flatness of the charged-current cross section at low $Q^2$. At higher values of $Q^2$, the charged-current cross section decreases more rapidly with $Q^2$ due to the $1/(m_W^2 + Q^2)$ dependence of the propagator.

The observed differences in the $e^-p$ and $e^+p$ charged-current cross sections can be understood in terms of the PDFs involved. At low $Q^2$, the cross sections are dominated by interactions with low-$x$ sea quarks and antiquarks. Because the sea quark PDFs are approximately the same for up- and down-quarks, the $e^-p$ and $e^+p$ cross sections given in (12.39) and (12.40) are roughly equal. Whereas at high $Q^2$, interactions with valence quarks become more important ($Q^2 = xys$) and therefore the $e^-p$ cross section is greater than that for $e^+p$ because $u_V(x) > d_V(x)$ and due to the presence of the factor of $(1 - y)^2$ multiplying $d(x)$ in (12.40).

From the $Q^2$ dependence of the $\gamma$ and W-boson propagators and the size of the QED and weak coupling constants,

$$\frac{\sigma_{\mathrm{NC}}^{QED}}{\sigma_{\mathrm{CC}}^{\mathrm{W}}} \sim \frac{\alpha^2}{\alpha_W^2} \cdot \frac{(Q^2 + m_{\mathrm{W}}^2)^2}{Q^4}.$$

Consequently, at low $Q^2$ the neutral-current cross section, which is dominated by photon exchange, is larger than weak charged-current cross section. However, for $Q^2 \gtrsim m_{\mathrm{W}}^2$, the photon and W-boson propagator terms are approximately equal and the observed convergence of the neutral-current and charged-current cross sections reflects the similar intrinsic strengths of the electromagnetic and weak interactions, $\alpha \sim 1/137$ and $\alpha_W \sim 1/30$. Hence, the high-energy $e^{\pm}p$ scattering data from HERA provide direct experimental evidence that the coupling constants of QED and the weak interaction are not very different.

Finally, it is worth noting that for $Q^2 \gtrsim m_Z^2$, the neutral-current cross section includes significant contributions from both γ- and Z-exchange diagrams. The contribution to the scattering amplitude from the Z boson leads to the observed small differences between the $e^-p$ and $e^+p$ neutral-current cross sections at high $Q^2$.

## Summary

The main aim of this chapter was to provide an introduction to cross section calculations for the weak charged-current. In the limit where the masses of the particles can be neglected, these calculations are relatively straightforward, since for each Feynman diagram only one helicity combination needs to be considered. In the limit where $Q^2 \ll m_W^2$, the W-boson propagator has little $Q^2$ dependence and the neutrino interaction cross sections are proportional to the laboratory frame neutrino energy. The total neutrino and antineutrino interaction cross sections per nucleon, assuming equal numbers of protons and neutrons, were found to be

$$\sigma^{\nu N} = \frac{G_F^2 m_N E_\nu}{\pi}\left[f_q + \frac{1}{3}f_{\overline{q}}\right] \quad \text{and} \quad \sigma^{\overline{\nu}N} = \frac{G_F^2 m_N E_{\overline{\nu}}}{\pi}\left[\frac{1}{3}f_q + f_{\overline{q}}\right].$$

The $1/(Q^2 + m_W^2)$ form of the W-boson propagator was evident in the discussion of $e^-p$ and $e^+p$ scattering, where both charged-current (W exchange) and neutral current (γ and Z exchange) processes contribute. The convergence of the charged-current and neutral-current cross sections provides a direct demonstration that the QED and weak coupling constants might be related, hinting at the unified electroweak theory described in Chapter 15.

## Problems

**12.1** Explain why the tau-lepton branching ratios are observed to be approximately

$$Br(\tau^- \to e^-\nu_\tau\overline{\nu}_e) : Br(\tau^- \to e^-\nu_\tau\overline{\nu}_\mu) : Br(\tau^- \to \nu_\tau + \text{hadrons}) \approx 1 : 1 : 3.$$

**12.2** Assuming that the process $\nu_e e^- \to e^- \nu_e$ occurs only by the weak charged-current interaction (i.e. ignoring the Z-exchange neutral-current process), show that

$$\sigma_{CC}^{\nu_e e^-} \approx \frac{2m_e E_\nu G_F^2}{\pi},$$

where $E_\nu$ is neutrino energy in the laboratory frame in which the struck $e^-$ is at rest.

**12.3** Using the above result, estimate the probability that a 10 MeV Solar $\nu_e$ will undergo a charged-current weak interaction with an electron in the Earth if it travels along a trajectory passing through the centre of the Earth. Take the Earth to be a sphere of radius 6400 km and uniform density $\rho = 5520\ \mathrm{kg\ m^{-3}}$.

**12.4** By equating the powers of $y$ in (12.34) with those in the parton model prediction of (12.20), show that the structure functions can be expressed as

$$F_2^{\nu p} = 2xF_1^{\nu p} = 2x\left[d(x) + \bar{u}(x)\right] \quad \text{and} \quad xF_3^{\nu p} = 2x\left[d(x) - \bar{u}(x)\right].$$

**12.5** In the quark–parton model, show that $F_2^{eN} = \frac{1}{2}(Q_u^2 + Q_d^2)F_2^{\nu N}$.
Hence show that the measured value of

$$F_2^{eN}/F_2^{\nu N} = 0.29 \pm 0.02,$$

is consistent with the up- and down-quarks having respective charges of $+\frac{2}{3}$ and $-\frac{1}{3}$.

**12.6** Including the contributions from strange quarks, the neutrino–nucleon scattering structure functions can be expressed as

$$F_2^{\nu p} = 2x[d(x) + s(x) + \bar{u}(x)] \quad \text{and} \quad F_2^{\nu n} = 2x[u(x) + \bar{d}(x) + \bar{s}(x)],$$

where $s(x)$ and $\bar{s}(x)$ are respectively the strange and anti-strange quark PDFs of the nucleon. Assuming $s(x) = \bar{s}(x)$, obtain an expression for $xs(x)$ in terms of the structure functions for neutrino–nucleon and electron–nucleon scattering

$$F_2^{\nu N} = \frac{1}{2}\left(F_2^{\nu p}(x) + F_2^{\nu n}(x)\right) \quad \text{and} \quad F_2^{eN} = \frac{1}{2}\left(F_2^{ep}(x) + F_2^{en}(x)\right).$$

**12.7** The H1 and ZEUS experiments at HERA measured the cross sections for the charged-current processes $e^- p \to \nu_e X$ and $e^+ p \to \bar{\nu}_e X$ for different degrees of electron longitudinal polarisation. For example, the ZEUS measurements of the total $e^+ p \to \bar{\nu}_e X$ cross section at $\sqrt{s} = 318$ GeV and $Q^2 > 200\ \mathrm{GeV}^2$ for positron polarisations of $P_e = -36\%$, 0% and +33% are:

$$\sigma(-0.36) = 22.9 \pm 1.1\,\mathrm{pb}, \;\; \sigma(0) = 34.8 \pm 1.34\,\mathrm{pb} \;\text{ and }\; \sigma(+0.33) = 48.0 \pm 1.8\,\mathrm{pb},$$

see Abramowicz *et al.* (2010) and references therein. Plot these data and predict the corresponding cross section for $P_e = -1.0$, i.e. when the positrons are all left-handed. What does this tell you about the nature of the weak charged-current interaction?